

Supplemental information for “Nanoscale imaging of light-matter coupling inside metal-coated cavities with a pulsed electron beam”

Robert J. Moerland,* I. Gerward C. Weppelman, Marijke Scotuzzi, and
Jacob P. Hoogenboom*

*Department of Imaging Physics, Delft University of Technology, NL-2600 GA Delft, The
Netherlands*

E-mail: r.j.moerland@tudelft.nl; j.p.hoogenboom@tudelft.nl

I. Experimental Setup

Our setup to measure time-resolved cathodoluminescence is shown in Fig. S1a. Items within the yellow boundary are placed inside the vacuum of a Scanning Electron Microscope (SEM). At the top, a Schottky source provides the electrons that make up the electron beam. Condensor lens C1 is used to set the current in the electron beam. The combination of the condensor lens C2 and the deceleration lens is modified such, that it focuses the electron beam in between the blanker plates. Finally, the electron objective lens images this focus onto the sample. Since the two foci are conjugated, the focus on the sample remains stationary while blanking.¹ The optical objective built into the SEM vacuum chamber is part of an optical microscope, with its tube lens outside of the chamber. Emission from the sample is focused onto an avalanche photo diode by the combination

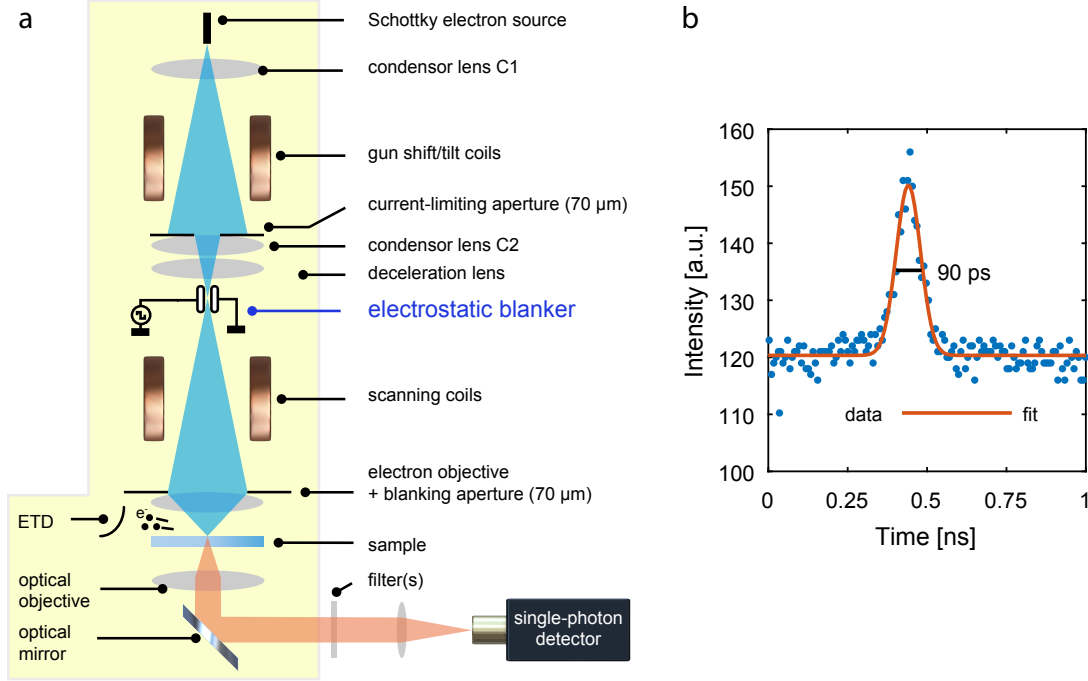


Figure S1: (a) Experimental setup to measure time-resolved cathodoluminescence. An electrostatic blinder in conjugated mode is used to sweep the electron beam over an aperture. This results in pulses of electrons, while maintaining a steady focus on the sample. b) An example of a bursts of electrons with a duration of about 90 ps full-width at half the maximum, obtained by a home-built streak camera. This duration is sufficiently short to enable the use of a time-correlated single-photon-counting scheme.

of objective and tube lens.

An example of the typical electron pulse length is shown in Fig S1b, obtained with a home-built streak camera. The pulse duration of about 90 ps full-width half-maximum is sufficiently short to use time-correlated single-photon counting techniques to establish the decay curve of typical emitters (here, Ce^{3+}).

II. Analytical Model of Nanocavity

We approximate the nanocavities, coated with aluminum and with an open end in the substrate, as a semi-infinite cylindrical waveguide with a circular cross-section. The side walls and the closure at one end of the waveguide are perfectly electrically conducting (PEC). We choose the z -axis such, that it is along the length of the semi-infinite waveguide. Dipoles are located at $z = 0$, at a distance

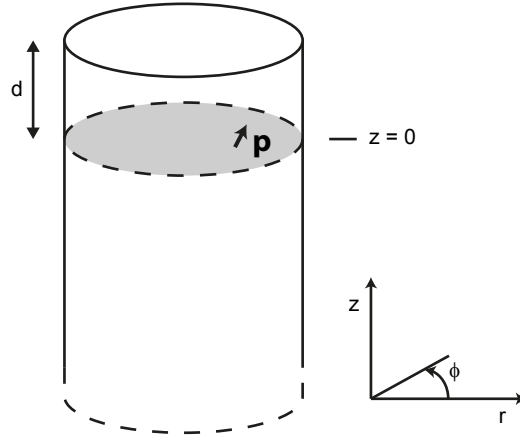


Figure S2: Cylindrical waveguide with circular cross-section. Dipoles are located at $z = 0$, where the distance to the PEC top of the cavity is defined by d .

d to the PEC closure (see Fig. S2). This way we take the electron scattering depth into account, as this allows us to calculate the decay rate of emitters at any location within the cavity. We use this in the convolution of the theoretical result with the PSF obtained in the previous section and explained in the main text.

By considering the metal coating as a perfect conductor, and neglecting the open end at the bottom of the cavity, we can consider our nanocavities as cylindrical waveguides with a circular cross section, closed off at one end with a perfect conductor (see Fig. S2). This allows us to analytically calculate the power emitted by a classical dipole into each available mode inside the cavity, as a function of location and orientation of the dipole. The (infinite) waveguide allows transverse magnetic (TM) and transverse electric (TE) modes, defined by $H_z = 0$ or $E_z = 0$, respectively. The solution for E_z for TM waves in this case is:²

$$E_z(r, \phi, z) = J_m(k_r r) \begin{Bmatrix} \sin m\phi \\ \cos m\phi \end{Bmatrix} e^{ik_z z}, \quad (\text{S1})$$

where k_z is the propagation constant of the mode, J_m is the Bessel function of the first kind where m is zero or a positive integer and the whole solution is subject to $J_m(k_r r) = 0$ at the boundary. This yields $k_r = \xi_{mn}/a$ with a the radius of the waveguide and ξ_{mn} the n -th zero of the Bessel

function of order m . The propagation constant k_z then becomes $k_z = (\omega^2 \mu \varepsilon - (\xi_{mn}/a)^2)^{1/2}$. Similarly, for TE waves

$$H_z(r, \phi, z) = J_m(k_r r) \begin{Bmatrix} \sin m\phi \\ \cos m\phi \end{Bmatrix} e^{ik_z z}, \quad (\text{S2})$$

now subject to $J'_m(k_r r) = 0$ where the prime indicates the derivative. Here, $k_r = \xi'_{mn}/a$ with ξ'_{mn} the n -th zero of the derivative of the Bessel function of order m . The tangential electric field components E_r and E_ϕ of the TM or TE modes can be obtained from E_z or H_z , respectively, with²

$$\mathbf{E}_t = \frac{1}{\omega^2 \mu \varepsilon - k_z^2} \left[\nabla_t \frac{\partial E_z}{\partial z} + i\omega \mu \nabla_t \times H_z \right],$$

where $\mathbf{E}_t = (E_r, E_\phi)$ and $\nabla_t = (\partial/\partial r, r^{-1}\partial/\partial\phi)$ in polar coordinates.

The power dissipated into each mode, by a current distribution \mathbf{J} present in a volume V , is given by the amplitude a_{mn} of that mode when excited by \mathbf{J} . The expression for the amplitude is:³

$$a_{mn} = -1/(4N_{mn}) \int_V \mathbf{E}^* \cdot \mathbf{J} dV \quad (\text{S3})$$

with $\mathbf{E} = (E_r, E_\phi, E_z)$ and N_{mn} a normalization constant given by

$$N_{mn} = \frac{1}{2} \int_S (\mathbf{E} \times \mathbf{H}^*) \cdot \hat{z} dS.$$

Integration is over the cross section S . Then, the power into any single mode is given by $P_{mn} = |a_{mn}|^2 N_{mn}$. To describe a dipole, we choose \mathbf{J} to be a current infinitesimally small in size, described by a three-dimensional delta function. Furthermore, without loss of generality, we choose $z = 0$ for the plane in which the dipole lies and $z = d$ for the plane where the cavity is closed off with a perfect conductor, see also Fig. S2. We apply the superposition principle between $z = 0$ and $z = d$ to construct a solution, consisting of waves propagating in the $+z$ and $-z$ direction, such that the tangential field (E_r, E_ϕ) is zero at $z = d$. Then, all boundary conditions are fulfilled.

This yields an expression for the total field at $z = 0$ which is inserted into Eq. S3, where we only have to take modes into account that propagate in the $-z$ direction. Hence, we can calculate the amount of power $P(r, \phi, z)$ that is dissipated by a classical dipole at a depth d underneath the metal closure of a nanocavity with arbitrary radius, and determine into which mode. We can relate this to the decay rate of a quantum emitter by using $P/P_0 = \gamma/\gamma_0$ where P_0 is the power dissipated by a classical dipole in a reference environment (here: an infinite YAG crystal) and γ_0 the decay rate of a quantum emitter in the same environment. We take Ce^{3+} as an isotropic emitter and therefore average the decay rates of dipoles oriented along the three orthogonal axes.⁴ We take the broad spectrum of Ce^{3+} in YAG into account by calculating the isotropic decay rates over the frequency range of interest and weighting it with the measured and normalized Ce^{3+} :YAG emission spectrum. Finally, as the cavities have a slight conical shape, i.e., the sidewalls are not exactly perpendicular to the substrate, we interpolate between the minimum and maximum radius of the cavity when we calculate the decay rate as a function of depth. This result is then used in the convolution with the electron point-spread function (see below).

III. Estimate of Cathodoluminescence Point-Spread Function

In order to estimate our point-spread function of the focused electron beam, we perform a Monte Carlo simulation of the elastic scattering of electrons with the freely-available software package CASINO.⁵ As a substrate we use Yttrium-Aluminum Garnet ($\text{Y}_3\text{Al}_5\text{O}_{12}$), where we use the manufacturer-provided density of 4.57 g/cm^3 .⁶ On top of the substrate, we place a layer of 30 nm thickness with the parameters of aluminum, as provided by the program. We simulate the scattering of 100,000 electrons and use that data to build a three-dimensional point-spread function (PSF). For every electron scattering event, the scattering position and energy loss is recorded. Subsequently, we discretize the scattering positions onto a grid of cubes of $5 \times 5 \times 5 \text{ nm}$, and determine the total number of scattering events and energy loss per mesh cube. We assume that the CL intensity is proportional to the electron energy loss due to elastic scattering,⁷ i.e., a constant fraction of

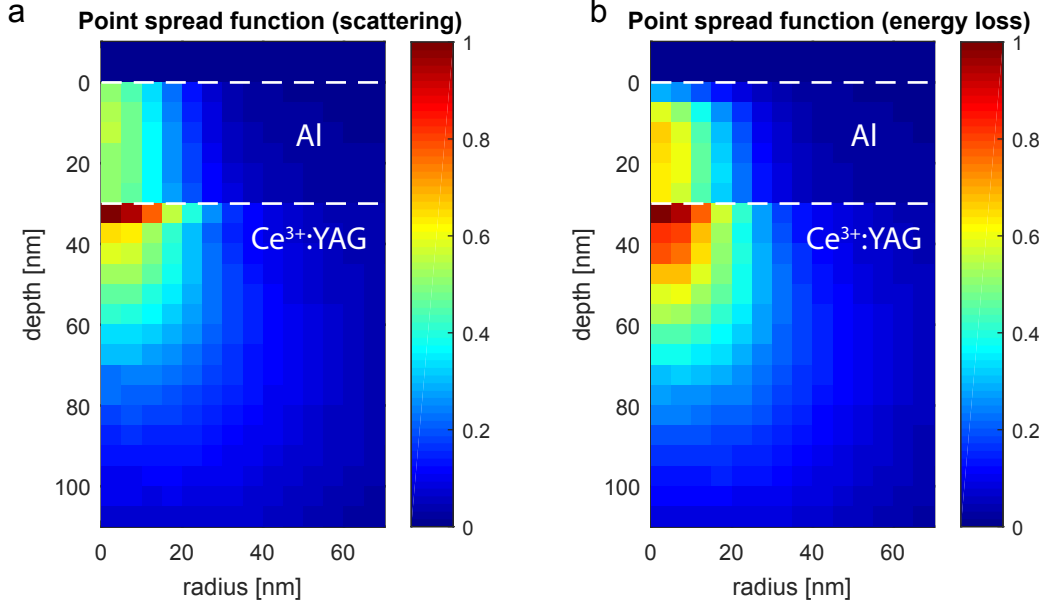


Figure S3: Monte-Carlo simulation (CASINO) of electron scattering in a YAG crystal, coated with 30 nm of aluminum. For display purposes only, and assuming symmetry along the z -axis (depth), the three-dimensional point-spread function (PSF) has been averaged over the polar coordinate ϕ , in the plane of the substrate. The profile as a function of radius and depth then describes the full PSF. In (a), the relative number of electron scattering events is plotted, whereas in (b), the relative energy loss is plotted per cell of 5×5 nm. With the assumption of proportionality between the CL intensity and the energy loss,⁷ the density of excited emitters is therefore equal to the PSF shown in panel (b).

the energy loss in any cube will lead to transitions of Ce^{3+} ions to the excited state, as detailed in the main text. Therefore, for any position of the electron beam, we take the density of excited Ce^{3+} emitters to be proportional to the energy loss distribution $E_{\text{loss}}(\mathbf{r})$ we obtained via this procedure, where \mathbf{r} is a vector iterating over all grid positions in the volume of the PSF.

We consequently define the interaction volume of the electron beam as that volume which contains half of the deposited energy (here: 2 keV), which results into a volume of $4.4 \cdot 10^{-4} \mu\text{m}^3$. The results of the Monte Carlo calculation are shown in Fig. S3, where for display purposes we have averaged the point-spread function in the angular direction. In Fig. S3a, the normalized number of scattering events is plotted, whereas in Fig. S3b the normalized energy loss per location is plotted, which is the data used for the convolution procedure.

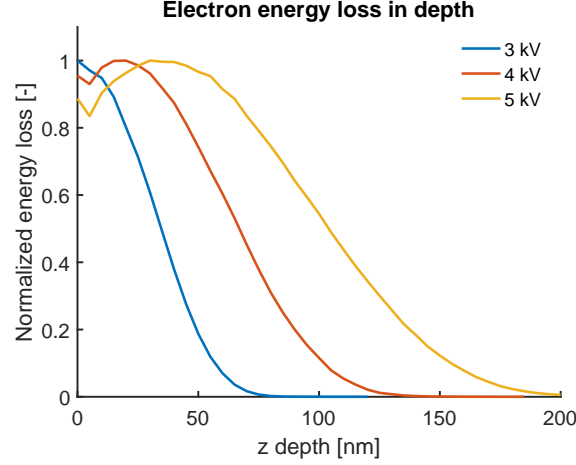


Figure S4: Energy loss distribution of electrons inside YAG, with 30 nm of aluminum on top for various acceleration voltages. The interface between aluminum and YAG is at $z = 0$. For higher voltages, the electrons penetrate deeper into the YAG and therefore can excite Ce^{3+} ions deeper inside the cavity.

IV. Depth dependence of decay rate

In the experiment and model, we scan the electron beam in the xy -plane. Therefore, experimentally, we obtain the modulation of the decay rate in the cavity in the xy -plane (convolved with the PSF) but the modulation along the z -direction is averaged. With tomographic techniques and by employing multiple acceleration voltages it may be possible to probe the depth dependence of the decay rate inside the cavities,⁸ as the electron energy loss profile is modified. To illustrate this, we perform Monte Carlo simulations similar to those described in Sect. III for 3, 4 and 5 kV acceleration voltages. Figure S4 shows the normalized energy loss in YAG as a function of depth for each acceleration voltage, where we integrated the electron loss in the xy -plane. As such, we ignore radial dependencies here for simplicity. From Fig. S4, it is clear that higher acceleration voltages lead to a larger penetration depth of the electrons into the YAG material.

In Fig. S5 we plot the decay rate inside the cavities as obtained through our analytical model on the axis of symmetry ($r = 0$, black curve). Here we have used the average diameter of each nanocavity, which is stated in the title of each subfigure between parentheses. The colored bands in Fig. S5 represent the distribution of the energy loss function inside the YAG crystal, where the opacity of the color is a measure for the amount of deposited energy, directly corresponding to the

curves in Fig. S4. The colored dots are simply the calculated average decay rate, weighted with the energy loss distribution of the electrons. The position of the data point on the x -axis is the average depth itself, weighted by the energy loss. In all cavities, the decay rate increases as a function of depth, which is also evident from the calculated average decay rate for the three acceleration voltages: as the voltage increases, a deeper part of the cavity is probed and as a result a higher average decay rate would be the result. Therefore, a rather naive implementation would already result in useful information on the decay rate distribution deeper down into the cavity. As such, it is plausible that with more advanced tomographic techniques the depth dependence of the decay rate can be further resolved.⁸

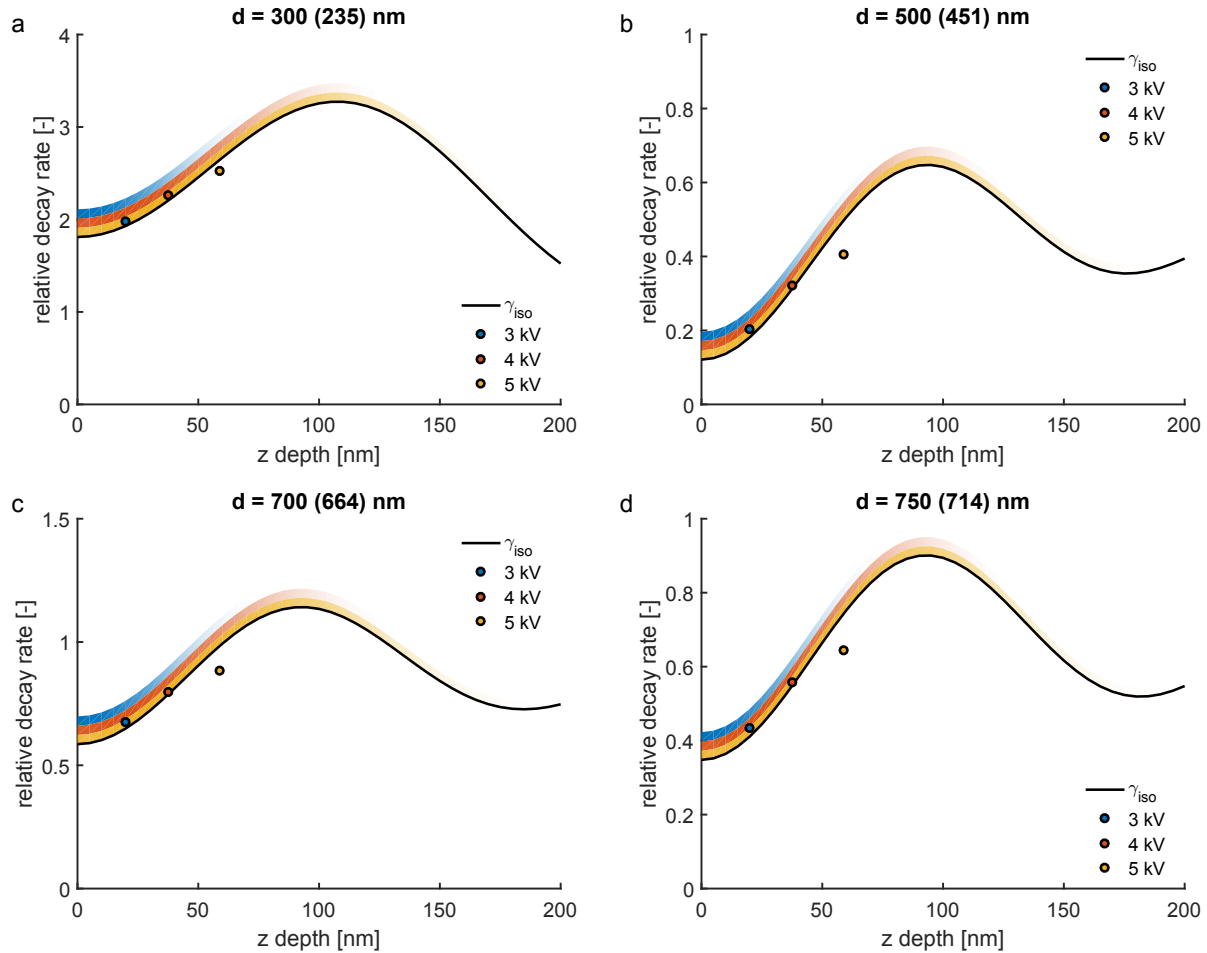


Figure S5: (a)–(d) Decay rate inside the cavities as obtained through our analytical model on the axis of symmetry ($r = 0$, black curve). Here, we used the average diameter of the cavities, indicated between parentheses behind the programmed thickness. The colored bands indicate the energy loss curves from Fig. S4, where the opacity is proportional to the energy loss. Larger acceleration voltages lead to a energy loss distribution that probes the deeper areas of the cavities. The colored dots are a calculation of the expected average decay rate, where the energy loss distribution was used for weighting. The depth position was calculated as a weighted average of the position in z . This simple approach shows that already then information about the decay rate variation in depth can be retrieved.

V. Non-radiative pathways

The model of Section II assumes perfect metal, i.e., lossless. Typically, some losses occur when emitters are very close to an absorbing medium, such as real metals due to either the generation of plasmons or direct non-radiative energy transfer.^{9,10} Due to limitations in time, we have performed a limited set of fully three-dimensional finite-element simulations for the smallest cavity in our data set. This cavity, with programmed size of 300 nm, is likely a good representative for a worst-case scenario as emitters are most closely surrounded by absorbing walls which quench the emission, and Q-factors in all cavities are moderate such that strongly resonantly enhanced losses can be neglected. Furthermore, we limited ourselves to simulations at the emission peak of Ce^{3+} in YAG, 550 nm. Figure S6a shows a cross section of the simulation domain, with in grey the aluminum walls of the nanocavity and in purple the YAG substrate. Above the substrate, the medium is vacuum. The conical shape is based on measurements with the electron microscope of the fabricated structure. We sweep a point dipole along the z -direction for $r = 0$, and perform a simulation for each of the two principal dipole orientations. The E_z part of the electric field is plotted in Fig. S6b for a certain moment in time, where the dipole is oriented along the z -axis and located 30 nm below the surface of the cavity.

The results of the sweep in z are shown in Fig. S7a. Here we plot the isotropic relative decay rate γ_{iso} as defined in the main text, and extract the (normalized) radiative and nonradiative parts γ_r and γ_{nr} , respectively. We see that the radiative decay rate is in qualitative agreement with our results obtained analytically. The non-radiative decay channels are initially high but diminish rapidly, which corresponds to quenching of the emitter by the aluminum layer. After this fast decay of the non-radiative decay rate due to near-field energy transfer, γ_{nr} slowly drops further which we attribute to the widening of the structure and therefore with a larger distance between the emitter and the walls, where radiatively-induced losses dominate.

For a depth of $z = 30$ nm into the cavity, where non-radiative energy transfer of radiation does not dominate anymore, we sweep the radial distance r and calculate γ_{iso} for each position in the sweep. The results are shown in Fig. S7b. Also here, γ_r is qualitatively in agreement with the

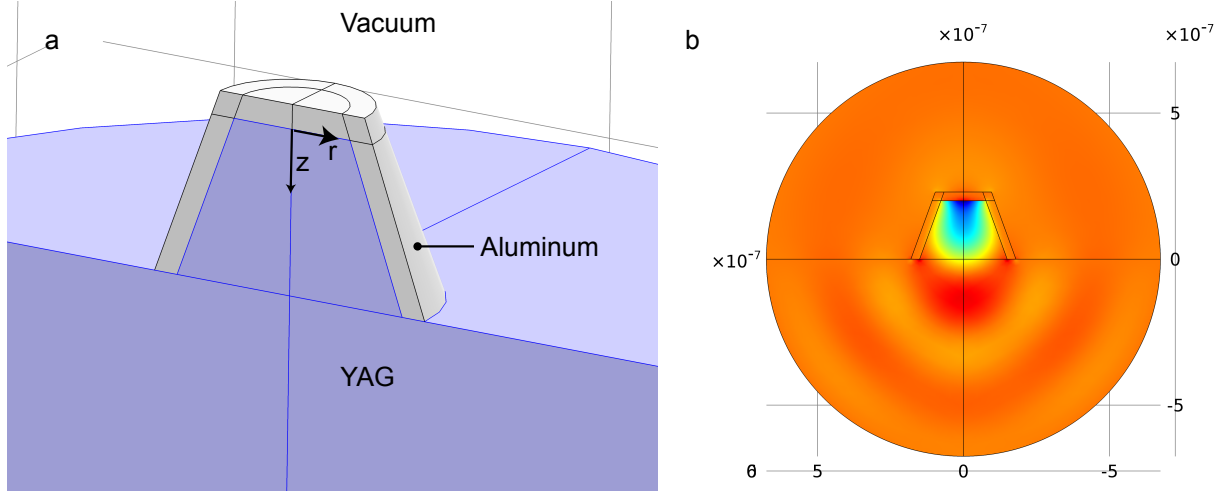


Figure S6: Three-dimensional finite-element simulations of a nanocavity in order to calculate the fraction of non-radiative pathways. (a) Cross section of the model. In purple, the YAG substrate and load of the cavity are shown ($n_{YAG} = 1.83$). The metal wall with a refractive index of $n_{Al} = 0.9643 + 6.3964i$ is shown in grey. The remainder of the domain is vacuum ($n = 1$). (b) The z -oriented part of the electric field E_z is shown for a specific moment in time, for a z -oriented dipole located on the axis of symmetry and 30 nm below the surface of the cavity. Here, we have taken the smallest cavity as a worst-case example.

analytical model. Furthermore, we see that γ_{nr} is relatively constant then, until again the emitter gets very close to the aluminum sidewall and quenching of emission is induced.

From the data in Fig. S7a and b, we can estimate the fraction of non-radiative pathways that are part of the total decay rate, as probed by the electron with an energy of 4 keV. For the typical depth of the electrons of 30–40 nm (see Fig. S5), this is about 35–40%, and not very sensitive to the radial position, except for at the edges of the cavity.

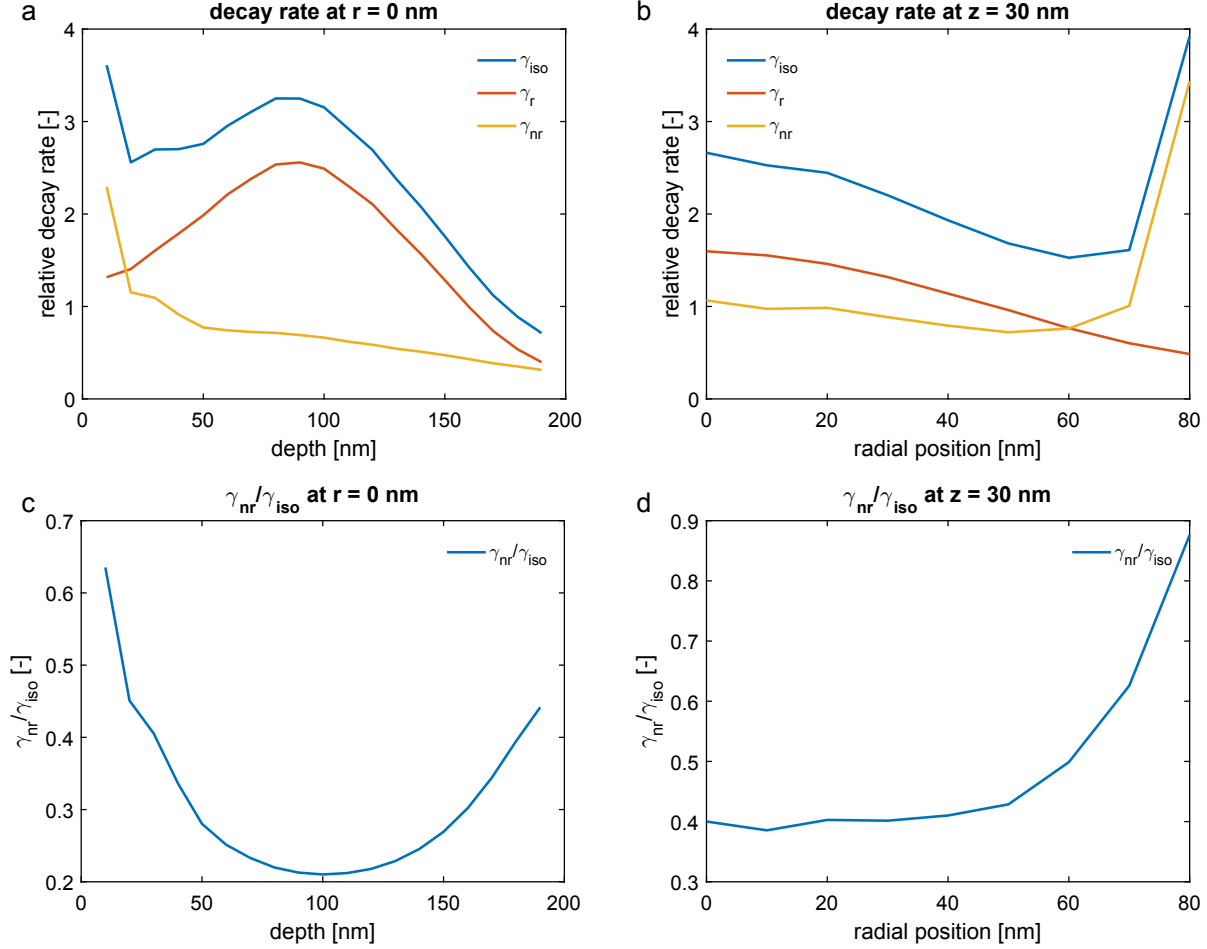


Figure S7: Isotropic relative decay rate γ_{iso} , and the radiative and non-radiative components for the cavity of 300 nm (see Fig. S6). In (a), we plot γ_{iso} (see main text), the radiative part of γ_{iso} named γ_r , and the non-radiative part γ_{nr} , where we swept the dipole position in depth while maintaining the radial position r at zero. In (b), we maintained a depth of 30 nm and swept the radial position r instead. Close to the metal walls, the non-radiative decay rate rises quickly due to non-radiative energy transfer to the metal. In (c) and (d), the corresponding fraction of the non-radiative decay channels is plotted, for a sweep in depth and radial position, respectively.

References

- (1) Moerland, R. J.; Weppelman, I. G. C.; Garming, M. W. H.; Kruit, P.; Hoogenboom, J. P. *Opt. Express* **2016**, *24*, 24760–24772.
- (2) Kong, J. *Electromagnetic Wave Theory*; A Wiley-Interscience publication; Wiley, 1986.
- (3) Snyder, A.; Love, J. *Optical Waveguide Theory*; Chapman and Hall, 1983.
- (4) Barnes, W. L. *J. Mod. Opt.* **1998**, *45*, 661–699.
- (5) Hovington, P.; Drouin, D.; Gauvin, R. *Scanning* **1997**, *19*, 1–14.
- (6) Material data provided by manufacturer: CRYTUR, spol. s r.o <http://www.crytur.cz>.
- (7) Toth, M.; Phillips, M. R. *Scanning* **1998**, *20*, 425–432.
- (8) Boughorbel, F.; Zhuge, X.; Potocek, P.; Lich, B. *Microsc. Microanal.* **2012**, *18*, 560–561.
- (9) Pockrand, I.; Brillante, A.; Möbius, D. *Chem. Phys. Lett.* **1980**, *69*, 499–504.
- (10) Hayashi, T.; Castner, T. G.; Boyd, R. W. *Chem. Phys. Lett.* **1983**, *94*, 461–466.